Chapter 2
Bending and Buckling Instabilities of Free Liquid Jets: Experiments and General Quasi-One-Dimensional Model

A.L. Yarin

Abstract This chapter deals with liquid jets bending due to the aerodynamic interaction with surrounding air or buckling due to the impingement on a solid wall. The experimental evidence is considered and linear and nonlinear theories describing perturbation growth developed in the framework of the quasi-one-dimensional equations of the dynamics of liquid jets moving in air are discussed. Jets of viscous Newtonian or rheologically complex liquids (in particular, viscoelastic polymeric liquids) are considered. In addition, bending instability of the electrified liquid jets (in particular, polymeric liquid jets in electrospinning) is considered. In the latter case, both the experimental and theoretical aspects are tackled.

Keywords Bending instability of liquid jets · Buckling of liquid jets · Electrified liquid jets · Electrospinning · Elongational rheology · Newtonian and rheologically complex liquids · Quasi-one-dimensional equations of the dynamics of liquid jets · Small and finite perturbations · Viscoelastic polymeric liquids

Introduction

Thin liquid jets demonstrate not only capillary breakup considered in Chap. 1 but some other regular long-wave forms of instability and breakup, e.g., bending instability of jets moving in air with a relatively high-speed U or of the electrified jets, as well as buckling of thin, highly viscous jets impinging on a wall [1]. Theoretical investigation of the dynamics of bending instability of liquid jets rapidly moving in air began in the seminal works of Weber and Debye and Daen [2, 3]. This leads to a rather complicated coupled problem on a dynamic interaction

A.L. Yarin
Department of Mechanical and Industrial Engineering, University of Illinois at Chicago, Chicago, IL, USA
e-mail: ayarin@uic.edu

N. Ashgriz (ed.), *Handbook of Atomization and Sprays*,
DOI 10.1007/978-1-4419-7264-4_2,

of air flow with a jet when the jet evolution is to be found as well. The linear stability analysis of the temporary planar bending instability of an inviscid jet in [3] resulted in the following characteristic equation for the growth rate γ of bending instability based on the three-dimensional equations of fluid mechanics

$$\gamma = \bar{k}\sqrt{-\frac{\rho_g U^2}{\rho a_0^2}\frac{K_1(\bar{k})I_1'(\bar{k})}{K_1'(\bar{k})I_1(\bar{k})} - \frac{\sigma}{\rho a_0^3}\frac{\bar{k}I_1'(\bar{k})}{I_1(\bar{k})}} \tag{2.1}$$

In (2.1) $\bar{k} = ka_0$ is the dimensionless wave number with k being the dimensional wave number and a_0 the unperturbed jet cross-sectional radius; ρ and σ are the density and surface tension of the jet liquid, respectively; the gas density is denoted by ρ_g; and I_1 and K_1 denote the modified Bessel functions. From several terms in the analysis of [3] describing the dynamic action of air, we keep in (2.1) only the largest one, of the order of $\rho_g U^2$, since $\rho_g << \rho$. The surface tension is a stabilizing factor in the case of the bending instability, since bending results in an increase of the jet surface area $[I_1'(\bar{k}) > 0,\ K_1'(\bar{k}) < 0$ for any $\bar{k}]$. Beginning from a certain critical value of the relative air velocity U, the first (positive) term under the square root on the right hand side in (2.1) acquires a larger magnitude than the second term, which corresponds to the onset of the bending instability and an exponential growth of the bending perturbations. The bending instability is determined by a peculiar pressure distribution in gas over the jet surface: in the framework of the inviscid gas model, gas pressure on convex surface elements is lower than on the concave ones.

General Quasi-One-Dimensional Equations of Dynamics of Free Liquid Jets

The theory of Debye and Daen [3] does not account for a number of important factors. The most important of them is the effect of liquid viscosity, which should counteract to the perturbation growth. In addition, the experiments show that the growing bending perturbations are three-dimensional rather than planar. Also, in the case of low-viscous liquid jets, bending perturbations grow together with the axisymmetric capillary perturbations, which significantly change the cross-sectional sizes and shapes during bending [4]. Moreover, all these factors are dominant in reality. Therefore, the analysis of the dynamics of the bending perturbations in the framework of an inviscid liquid model is intrinsically contradictory. Accounting for these factors in the framework of the Navier–Stokes equations in the context of the bending perturbations of liquid jets is tremendously difficult. However, these difficulties can be relatively easily overcome in the framework of the quasi-one-dimensional description of liquid motion in the bending jets. In the works of Yarin et al. [1, 5, 6], the general quasi-one-dimensional equations of the straight and bending jets were derived from the integral balances of mass, momentum, and moment of momentum,

as well as by averaging the three-dimensional equations of hydrodynamics over the jet cross-section [7]. The quasi-one-dimensional continuity and momentum equations, as well as the moment of momentum equation for the general case of motion of a thin liquid jet in air derived by Yarin et al. [1, 5–7] read

$$\frac{\partial \lambda f}{\partial t} + \frac{\partial W f}{\partial s} = 0, \quad f = \pi a^2, \tag{2.2}$$

$$\frac{\partial \lambda f \vec{V}}{\partial t} + \frac{\partial W f \vec{V}}{\partial s} = \frac{1}{\rho}\frac{\partial}{\partial s}\left(P\vec{\tau} + \vec{\mathrm{Q}}\right) + \lambda \vec{F} f + \vec{q}\frac{\lambda}{\rho}, \tag{2.3}$$

$$\begin{aligned}\frac{\partial \lambda \vec{\mathrm{K}}}{\partial t} + \lambda\left[\vec{\tau} \times \vec{\mathrm{j}}_2 - k\vec{\mathrm{U}} \times \left(\vec{\Omega} \times \vec{\mathrm{j}}_1 + \delta\vec{\mathrm{j}}_1\right)\right] + \frac{\partial}{\partial s}\left(W\vec{\mathrm{K}}_1 + \vec{\mathrm{j}}_3 \times \vec{\mathrm{V}}\right) \\ = \frac{1}{\rho}\frac{\partial \vec{\mathrm{M}}}{\partial s} + \frac{\lambda}{\rho}\vec{\tau} \times \vec{\mathrm{Q}} + \vec{\mathrm{m}}\frac{\lambda}{\rho} - \lambda k\vec{\mathrm{j}}_1 \times \vec{\mathrm{F}}\end{aligned} \tag{2.4}$$

These equations are a close hydrodynamic analog of the equations of the Euler-Bernoulli beam theory [8]. They are related to the three-dimensional equations of hydrodynamics (the Navier–Stokes equations in the case of viscous Newtonian liquids) exactly as the equations of the Euler-Bernoulli beam theory are related to the three-dimensional equations of the theory of elasticity. The hydrodynamics of thin liquid jets is reduced to finding the evolution in time t and over a spatial coordinate s of the "integral" parameters – the cross-sectional area f, the velocity of the center of mass of a liquid cross-section $\vec{\mathrm{V}}$, and the angular velocity of this cross-section $\vec{\Omega}$. Equation (2.2) is the mass balance (the continuity equation). Equation (2.3), the momentum equation, represents itself the balance of forces acting on a jet element, namely, the inertial, internal and external forces. Equation (2.4) represents itself the moment of momentum balance, in particular, its left-hand side expresses the rate of change of the moment of the inertial forces. The following notation is used in (2.2)–(2.4)

$$\vec{\mathrm{K}} = \int\limits_D \left(\vec{\mathrm{x}} \times \vec{\Omega} \times \vec{\mathrm{x}}\right) dS - k\vec{\mathrm{j}}_1 \times \vec{\mathrm{V}}, \quad \vec{\mathrm{K}}_1 = \int\limits_D \left(\vec{\mathrm{x}} \times \vec{\Omega} \times \vec{\mathrm{x}}\right) dS, \tag{2.5}$$

$$\vec{\mathrm{j}}_1 = \int\limits_D y\vec{\mathrm{x}} dS, \quad \vec{\mathrm{j}}_2 = \int\limits_D \left(\vec{\Omega} \times \vec{\mathrm{x}} + \delta\vec{\mathrm{x}}\right)\left[\left(\vec{\Omega} - \vec{\omega}\right) \cdot (\vec{\mathrm{x}} \times \vec{\tau})\right] dS, \tag{2.6}$$

$$\vec{\mathrm{j}}_3 = \int\limits_D \vec{x}\left[\left(\vec{\Omega} - \vec{\omega}\right) \cdot (\vec{\mathrm{x}} \times \vec{\tau})\right] dS, \quad \lambda = \left|\frac{\partial \vec{\mathrm{R}}}{\partial \mathrm{s}}\right| \tag{2.7}$$

$$\vec{\mathrm{U}} = \frac{\partial \vec{\mathrm{R}}}{\partial t}, \quad W = V_\tau - U_\tau, \quad \delta = -\frac{1}{2}\left(\frac{1}{\lambda}\frac{\partial V_\tau}{\partial s} - kV_n\right) \tag{2.8}$$

Here, $\vec{\mathrm{R}}$ and $\vec{\mathrm{x}}$ denote the position vectors of the jet axis, and of a point in the jet cross-section, respectively ($\vec{\mathrm{x}}$ is reckoned from the center of mass of a jet cross-section $D(s, t)$ and belongs to its plane); $\vec{\mathrm{F}}$ is the body force per jet element of unit volume; $\vec{\mathrm{q}}$ and $\vec{\mathrm{m}}$ are the distributed force and moment of force imposed on the jet by the environment, respectively; $\vec{\mathrm{Q}}$ is the shearing force acting in the jet cross-section, which is determined using (2.4); k is the jet axis curvature; ρ is liquid density. Here and hereinafter, $\vec{\mathrm{n}}$, $\vec{\mathrm{b}}$, and $\vec{\tau}$ denote the principal unit normal, unit binormal, and unit tangent to the jet axis, respectively. The angular velocity of the trihedron $\vec{\mathrm{n}}$, $\vec{\mathrm{b}}$ and $\vec{\tau}$ associated with the jet axis is denoted $\vec{\omega}$. Subscripts n, b, and τ denote projections on the principal normal, binormal, and tangent to the jet axis, respectively; y is the coordinate reckoned along the principal normal. In the case of Newtonian viscous liquid, the magnitude of the longitudinal force in the jet cross-section P and the moment of the internal stresses $\vec{\mathrm{M}}$ are related to the kinematic parameters in a cross-section of radius a by the following expressions

$$P = \left[3\mu\left(\frac{1}{\lambda}\frac{\partial V_\tau}{\partial s} - kV_\mathrm{n}\right) - \sigma G\right]f + P_\sigma, \tag{2.9}$$

$$G = \frac{1}{a}\left[1 + \frac{1}{\lambda^2}\left(\frac{\partial a}{\partial s}\right)^2\right]^{-1/2} - \left[1 + \frac{1}{\lambda^2}\left(\frac{\partial a}{\partial s}\right)^2\right]^{-3/2}\frac{1}{\lambda}\frac{\partial}{\partial s}\left(\frac{1}{\lambda}\frac{\partial a}{\partial s}\right), \tag{2.10}$$

$$P_\sigma = 2\pi a\sigma\left[1 + \frac{1}{\lambda^2}\left(\frac{\partial a}{\partial s}\right)^2\right]^{-1/2}, \tag{2.11}$$

$$M_\mathrm{n} = 3\mu I\left(\frac{1}{\lambda}\frac{\partial \Omega_\mathrm{n}}{\partial s} + k\Omega_\tau - \kappa\Omega_\mathrm{b}\right) \tag{2.12}$$

$$\begin{aligned} M_\mathrm{b} = {} & 3\mu I\left(\frac{1}{\lambda}\frac{\partial \Omega_\mathrm{b}}{\partial s} + \kappa\Omega_\mathrm{n} - \frac{3}{2}\frac{k}{\lambda}\frac{\partial V_\tau}{\partial \mathrm{s}} + \frac{3}{2}k^2 V_\mathrm{n}\right) \\ & - \sigma k\frac{I}{a}\left[1 + \frac{1}{\lambda^2}\left(\frac{\partial a}{\partial s}\right)^2\right]^{-3/2} \end{aligned} \tag{2.13}$$

$$M_\tau = \mu I\left(\frac{2}{\lambda}\frac{\partial \Omega_\tau}{\partial s} + \frac{k}{\lambda}\frac{\partial V_\mathrm{b}}{\partial s} + k\kappa V_\mathrm{n} - k\Omega_\mathrm{n}\right), \quad I = \frac{\pi a^4}{4}, \tag{2.14}$$

Here, κ is the geometric torsion of the jet axis, μ and σ are the viscosity and surface tension coefficient, respectively, and I is the moment of inertia of the jet cross-section.

The system of (2.2)–(2.14) describes both the axisymmetric capillary instability of straight jets ((1.49)–(1.51) in Chap. 1 represent its particular case) and bending instability of liquid jets. It is closed if the jet cross-sections possess double symmetry (in particular, it is closed for jets with circular cross-sections). This system of equations was derived by Yarin et al. in [1, 5–7] assuming the jet slenderness and the absence of significant shear tractions at its surface. These assumptions are sufficiently accurate in the case of highly viscous jets moving in air. In the cases of short wavelength perturbations and large axis curvatures, as well as in the case of liquid jets propagating in liquid medium of comparable viscosity, the quasi-one-dimensional description, strictly speaking, is inappropriate. The assumptions of the jet slenderness and of the absence of significant shear tractions at the jet surface lead to the following additional restrictions on the internal kinematics in the jet, namely to

$$\Omega_{\mathrm{n}} = -\frac{1}{\lambda}\frac{\partial V_{\mathrm{b}}}{\partial s} - \kappa V_{\mathrm{n}}, \quad \Omega_{\mathrm{b}} = \frac{1}{\lambda}\frac{\partial V_{\mathrm{n}}}{\partial s} - \kappa V_{\mathrm{b}} + \kappa V_{\tau}, \tag{2.15}$$

The kinematic equation, which should be added to the system of (2.2)–(2.15), determines the location of the jet axis in space in accordance with the velocity field in it

$$\frac{\partial \vec{\mathrm{R}}}{\partial t} = \vec{\mathrm{V}} - (\lambda \vec{\mathrm{V}} \cdot \vec{\mathrm{i}})\vec{\tau} \tag{2.16}$$

Equation (2.16) is written here for the simplest case where the tangent to the jet axis is inclined at any point to a certain straight line $O_1\xi$ by an acute angle and it is possible to introduce a Cartesian coordinate system $O_1\xi\eta\zeta$ with the corresponding unit vectors $\vec{\mathrm{i}}$, $\vec{\mathrm{j}}$ and $\vec{\mathrm{k}}$ and to describe the jet axis using the following equations

$$\xi = s, \quad \eta = H(s,t), \quad \varsigma = Z(s,t), \quad \vec{\mathrm{R}} = \vec{\mathrm{i}}\,\xi + \vec{\mathrm{j}}H + \vec{\mathrm{k}}Z \tag{2.17}$$

In the other cases, the jet axis parameter s can be chosen differently, which leads to changes in the expression for $\partial\vec{\mathrm{R}}/\partial t$.

The distributed force and moment of force imposed on the jet by the environment $\vec{\mathrm{q}}$ and $\vec{\mathrm{m}}$ should be specified separately. In particular, in the case of small spatial perturbations of the jet axis when it rapidly moves in air, the inviscid flow theory yields the following expressions

$$\vec{\mathrm{q}} = -\rho_g U^2 f_0 \left(\vec{\mathrm{j}}\frac{\partial^2 H}{\partial s^2} + \vec{\mathrm{k}}\frac{\partial^2 Z}{\partial s^2}\right), \quad \vec{\mathrm{m}} = 0, \quad f_0 = \pi a_0^2, \tag{2.18}$$

Equation (2.18) for $\vec{q}$ means that it is directed along the normal (as $-\vec{n}$).

For the finite bending perturbations, the drag force imposed by a relative air flow should be accounted in addition. Then, for example, for planar jet bending, (2.18) are generalized by the following expressions

$$\vec{q} = -\rho_g U^2 \left\{ f \frac{\partial^2 H}{\partial s^2} \left[1 + \left(\frac{\partial H}{\partial s} \right)^2 \right]^{-5/2} + a \left(\frac{\partial H}{\partial s} \right)^2 \left[1 + \left(\frac{\partial H}{\partial s} \right)^2 \right]^{-1} \times \operatorname{sgn} \left(\frac{\partial H}{\partial s} \right) \right\} \vec{n}, \quad \vec{m} = 0 \tag{2.19}$$

These expressions close the system of the general quasi-one-dimensional equations of free liquid jets moving in air with arbitrary speeds.

In the context of the electrified jets in electrospraying and electrospinning, the distributed force $\vec{q}$ originates from the Coulomb repulsion of different parts of the jet surface. Then, it is given by the following expression [9–11]

$$\vec{q} = -e^2 \ln \left(\frac{L}{a} \right) k \vec{n} \tag{2.20}$$

where e is the electric charge at the jet surface per unit jet length and L is a cutoff length along the jet axis. Comparison of (2.18) and (2.20) shows that both the aerodynamic and electric bending forces are directed along the normal (as $-\vec{n}$) and should result in a very similar aerodynamically or electrically driven bending instability, as discussed below.

Linear Stability Theory for Bending Breakup of Newtonian Liquid Jets Moving in Air

The solutions of a particular version of the quasi-one-dimensional equations of the jet dynamics in the case of capillary breakup, when they can be reduced to (1.49)–(1.51) of Chap. 1, were discussed there. Here, we discuss the applications of (2.2)–(2.19) to the aerodynamically-driven bending instability of the uncharged liquid jets rapidly moving in air following the work of Yarin [1, 5, 6]. The characteristic equation for the growth rate of small bending perturbations of highly viscous slender liquid jets moving in air in the case of the temporal instability reads

$$\gamma^2 + \frac{3}{4} \frac{\mu \overline{k}^4}{\rho a_0^2} \gamma + \left(\frac{\sigma}{\rho a_0^3} - \frac{\rho_g U^2}{\rho a_0^2} \right) \overline{k}^2 = 0 \tag{2.21}$$

According to (2.21), both planar and three-dimensional (helical) small bending perturbations increase with the same growth rate if the relative velocity of gas flow is

$$U > \sqrt{\frac{\sigma}{\rho_g a_0}} \tag{2.22}$$

when the dynamic action of air can overbear the resistance of surface tension to growth of bending perturbations. The growth rate of the axisymmetric capillary perturbations is much smaller than that of the bending perturbations for sufficiently viscous liquids when the inequality

$$\frac{\mu^2}{\rho a_0^2 \rho_g U^2} \gg 1 \tag{2.23}$$

holds. In this case, deformations of the jet due to the capillary Rayleigh-Weber instability can be neglected during bending.

It is worth noting that at $\mu = 0$ (2.21) coincides with the long-wave limit ($\bar{k} \to 0$) of (2.1).

The breakup length of jets in the case of the aerodynamically-driven bending instability is determined by the following expression [1, 6]

$$L_{breakup} = \Delta \cdot \left[\frac{3\mu\rho a_0^2 U^3}{(\rho_g U^2 - \sigma/a_0)^2}\right]^{1/3} \tag{2.24}$$

where $\Delta = \ln(ma_0/\zeta_0)$, $m = 2$–4, ζ_0 is the initial amplitude of bending perturbations. The value of the factor m is chosen in agreement with the experimental data [4] and the energy estimates, which show that as the bending perturbation amplitude reaches the value of the order of a few cross-sectional radii, the jet is almost immediately squeezed by the air pressure difference at its surface. Equation (2.24) predicts a decrease in the jet breakup length at higher flow velocity U, which agrees with the experimental data. (It is emphasized that the breakup length $L_{breakup}$ of straight capillary jets experiencing Rayleigh-Weber instability increases proportionally to U).

Nonlinear Theory of Finite Bending Perturbations of Liquid Jets Moving in Air

In the works of Yarin [1, 6], the aerodynamically-driven nonlinear bending instability of thin jets of highly viscous liquids rapidly moving in air was studied numerically by solving (2.2)–(2.19). It was shown that the nonlinear effects, in

particular, the most important of them – the viscous stresses originating from the elongation of the bending jet axis – decelerate growth of bending perturbations. However, for the estimates of the perturbation amplitudes and timing up to the amplitudes of the order of (2–4)a_0 one may extrapolate the predictions of the linear theory with sufficient accuracy [as it was done in derivation of (2.24)]. The presence in (2.19) for $\vec{q}$ of the quadratic drag force leads to a slow sweep of bending perturbations down the gas flow in addition to growth of their amplitude (the latter is due to the "lift" component of the aerodynamic force $\vec{q}$). The configurations of the jet axis corresponding to one length of the bending perturbation at several consecutive time moments denoted by numerals by the curves are shown in Fig. 2.1. It is seen that the jet axis at the end takes a form of a cliff which leads to an "overturning." At this moment, the amplitude of the bending perturbation is of the order of $4a_0$. Figure 2.2 depicts the corresponding jet section at the moment of "overturning."

The rate of growth of the bending perturbations, as well as its deceleration due to the nonlinear effect (the longitudinal viscous stresses resulting from stretching of the jet axis at the nonlinear stage of bending) can be also calculated based on the energy balance given by Yarin [1]. Namely, the work of the distributed aerodynamic bending force $\vec{q}$ is spent on changes in the kinetic and surface energies and viscous dissipation in the jet. Assuming sinusoidal shape of a bending section of a jet, one arrives at the following equation for the amplitude $H(t)$ of the bending perturbation

$$H'' + \frac{3}{4}\frac{\mu}{\rho a_0^2}\bar{k}^4 H' + \frac{9}{4}\frac{\mu}{\rho a_0^4}\bar{k}^4 H^2 H' + H\bar{k}^2\left(\frac{\sigma}{\rho a_0^3} - \frac{\rho_g U^2}{\rho a_0^2}\right) = 0 \tag{2.25}$$

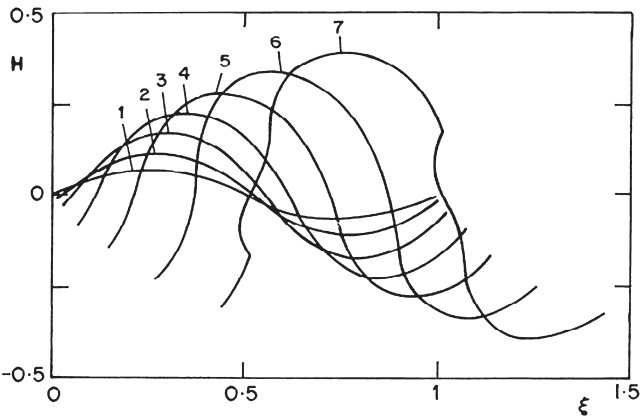

Fig. 2.1 Jet evolution in the case of the bending perturbations of finite amplitude affected by air drag force [1]. All the parameters in the plot are dimensionless. As a length scale, the wavelength of the fastest growing bending mode in the linear approximation $l_* = 2\pi\left[(9/8)\mu^2 a_0^4/\left(\rho\rho_g U^2\right)\right]^{1/6}$ is chosen. Time denoted by the numerals near the curves is rendered dimensionless by the characteristic time of small bending perturbations, $T = \left[\left(\rho\mu a_0^2\right)/\left(\rho_g^2 U^4\right)\right]^{1/3}$ (Courtesy of Pearson Education)

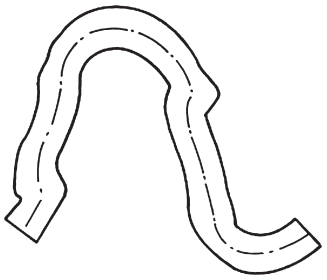

Fig. 2.2 Predicted instantaneous shape of a jet with a large-scale aerodynamically-driven bending instability corresponding to the jet axis configuration at $t = 7$ in Fig. 2.1 [1]. The cross-sectional radius ranging from 65% to 80% of its initial value (Courtesy of Pearson Education)

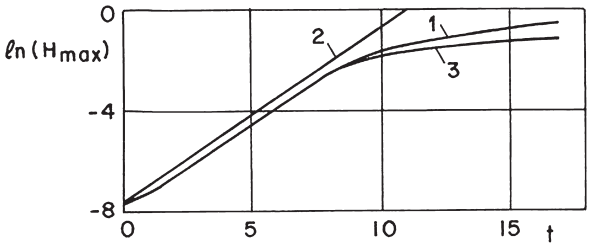

Fig. 2.3 The amplitude of the bending perturbation of a Newtonian liquid jet with $\mu = 1$ Pa s [1]. Curve 1 was obtained by solving the complete system of the quasi-one-dimensional equations of the jet dynamics (2.2)–(2.19). The straight line 2 corresponds to the linear theory: $H = H_0 \exp(\gamma t)$ with γ found from (2.21). Curve 3 was obtained by numerical integration of the nonlinear energy balance, (2.25). The length scale is taken as $l_* = 0.943 \times 10^{-2}$ m and $T = 0.0047$ s is used as a time scale (Courtesy of Pearson Education)

In (2.25) primes denote time differentiation. The above-mentioned nonlinear effect related to stretching of the jet axis by finite bending perturbations is given by the third (nonlinear in H) term on the left-hand side in (2.25). The linearized version of (2.33) corresponds to small bending perturbations and readily admits the solution $H = \exp(\gamma t)$. The amazing fact is that the growth rate γ thus obtained satisfies the exact (2.21). The nonlinear numerical solution of (2.25) is depicted in Fig. 2.3 together with the numerical solution of the quasi-one-dimensional equations and the result of the linear theory.

Bending Instability of Rheologically Complex Liquid Jets

Capillary instability and breakup of thin jets of dilute polymer solutions considered in section Capillary Breakup of Rheologically Complex Liquid Jets of Chap. 1 represents itself an example of the so-called strong flows, in which coil-stretch transition of macromolecular coils can happen because the elongation rate is so

high that viscoelastic relaxation does not succeed to fully unload the liquid. The corresponding presence of significant elastic stresses results in such peculiar non-Newtonian phenomena as formation of the beads-on-a-string structure. Bending instability of non-Newtonian liquids, in particular, of concentrated polymer solutions and melts, also reveals a wide spectrum of nontrivial deviations from the Newtonian behavior, related to a number of important applications. Some of them are discussed below.

The bending instability of jets of power law liquids rapidly moving in air was studied by Yarin [1] in the framework of the energy balance similar to the one which led to (2.25). An equation for the bending amplitude H obtained, which generalizes (2.25) for the power law liquids, reveals that the evolution of the bending perturbations of pseudoplastic jets ($n < 1$) is dominated by an initial stage where the perturbation amplitude and rates of deformation are small (similar to the capillary breakup of pseudoplastic jets discussed in Ch.1). On the other hand, in bending of dilatant ($n > 1$) high-speed jets, an increase of the effective viscosity at a later stage significantly decelerates perturbation growth.

The dynamics of bending perturbations of high-speed viscoelastic jets of uncharged polymer solutions and melts, as well as of concentrated micellar solutions was studied by Yarin [1]. One of the important applications of such jets is in melt blowing – a technology used to produce nonwoven mats of polymer nanofibers [12]. In Yarin [1], it was shown that the growth rate of small bending perturbations is determined by the following characteristic equation

$$\gamma^2 + \frac{3}{4}\frac{\mu\bar{k}^4}{\rho a_0^2(1+\gamma\theta)}\gamma + \left(\frac{\sigma}{\rho a_0^3} - \frac{\rho_g U^2}{\rho a_0^2} + \frac{\sigma_0}{\rho a_0^2}\right)\bar{k}^2 = 0 \tag{2.26}$$

which generalizes (2.21) to the case of viscoelastic liquid jets (the Newtonian case is recovered with the relaxation time $\theta = 0$). In (2.26) the initial longitudinal stress in the jet can either be absent ($\sigma_0 = 0$) or present and "frozen" $\sigma_0 = \text{const} \neq 0$.

If $\sigma_0 = 0$, (2.26) predicts an accelerated growth of small bending perturbations of viscoelastic liquids compared to a corresponding Newtonian liquid (with the same values of ρ, μ, σ, a_0, and U) due to a decrease in the effective viscosity $\mu_{\text{eff}} = \mu/(1 + \gamma\theta)$. The initial stress $\sigma_0 > 0$ is a stabilizing factor, which diminishes the growth rate γ, or can even prevent bending instability if $(\sigma_0 + \sigma/a_0) > \rho_g U^2$. The following dimensionless groups govern the bending perturbations of viscoelastic jets

$$\Pi_1 = \frac{\rho_g}{\rho},\quad \Pi_2 = \frac{\mu^2}{\rho a_0^2 \rho_g U^2},\quad \Pi_3 = \frac{\rho_g U^2}{\mu/\theta},\quad \Pi_4 = \frac{\sigma_0}{\rho_g U^2},\quad \Pi_5 = \frac{\sigma/a_0}{\rho_g U^2}, \tag{2.27}$$

Figure 2.4 depicts the growth rates predicted from (2.26) for two jets of the upper-convected Maxwell liquids, which are shown by curves 1 and 3. They correspond to different values of the relative gas velocity (U for curve 1 is higher

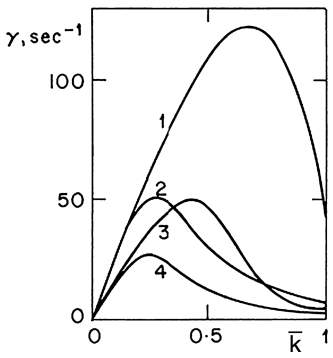

Fig. 2.4 Growth rate of small bending perturbations of viscoelastic jets of the upper-convected Maxwell liquid [1]. For all curves $\Pi_1 = 10^{-3}$, $\Pi_4 = \Pi_5 = 0$. For curves 1 and 2: $\Pi_2 = 0.156 \times 10^4$; for curves 3 and 4 $\Pi_2 = 0.4 \times 10^4$. For curves 2 and 4 $\Pi_3 = 0$. For curves 1 and 3 $\Pi_3 = 0.64$ and $\Pi_3 = 0.25$, respectively (Courtesy of Pearson Education)

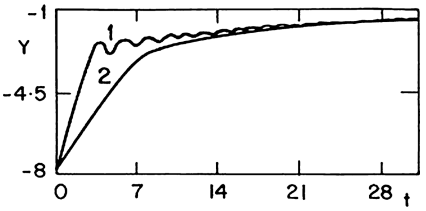

Fig. 2.5 The amplitude Y of the bending perturbations of a jet of the upper-convected Maxwell liquid is shown by curve 1 [1]. The values of the dimensionless groups are: $\Pi_1 = 10^{-3}$, $\Pi_2 = 0.156 \times 10^4$, $\Pi_3 = 0.64$, $\Pi_4 = \Pi_5 = 0$. Curve 2 depicts the amplitude of the corresponding jet of Newtonian liquid ($\Pi_3 = 0$) (Courtesy of Pearson Education)

than for curve 3). Curves 2 and 4 show the results for the corresponding Newtonian liquid jets, with curve 2 corresponding to curve 1, and curve 4 to curve 3.

The nonlinear dynamics of the bending perturbations of high-speed viscoelastic uncharged jets moving in air reveals a new phenomenon found by Yarin [1]. Figure 2.5 shows that at the nonlinear stage the growth of the perturbation amplitude is not only drastically slowed down due to the longitudinal stresses resulting from the jet elongation (similar to Newtonian jets discussed above), but the amplitude can also decrease and oscillate. These latter phenomena result from the competition of the inertial and elastic forces. A jet element undergoing bending misses its "equilibrium" position due to its inertia, and the jet axis becomes overstretched, which produces an extra longitudinal elastic stress. This stress tends to contract the jet element. However, during the contraction stage (when the bending perturbation amplitude decreases), the jet element once more misses its "equilibrium" position due to its inertia and becomes overcompressed. This initiates a new cycle of the oscillations. Viscous stresses gradually dissipate the energy of these oscillations.

Buckling of Thin Liquid Jets

G.I. Taylor in his seminal works [13, 14] discovered a new instability mode of highly viscous jets, namely buckling of slowly moving jets impinging onto a wall when they are subjected to a longitudinal compressive force. In one of his experiments, compressive forces resulted from squeezing the ends of a liquid thread floating on the mercury surface. In another experiment, highly viscous jets were either moving vertically downward in a liquid and passing into a lower layer of higher density, which created a sudden increase in the compressive buoyancy force, or impinging onto a wall. The latter case was experimentally studied in detail in [15, 16]. These works showed that buckling occurs only in very slowly moving highly viscous jets. The jets with the values of the Reynolds number Re exceeding the critical threshold of $\mathrm{Re}_{\mathrm{cr}} \approx 1.2$ were stable and straight. Therefore, in this case, the buckling instability emerges when the Reynolds number decreases. On the other hand, there is also a restriction on the jet lengths L from nozzle to wall. If L is less than a certain critical value L_{cr}, there is no buckling. Immediately after the onset of the buckling instability (at $\mathrm{Re} \leq \mathrm{Re}_{\mathrm{cr}}$ and $L/d_0 \geq L_{\mathrm{cr}}/d_0$ with d_0 being the nozzle diameter) a two-dimensional bucking (folding) sets in, and the jet is deposited on the wall as folds. However, with a further increase of the ratio L/d_0, bucking perturbations become spiral-like. The jet axis becomes three-dimensional, which signifies the bifurcation from folding to coiling, and the jet is deposited on the wall as coils. In the experiments [15], the dependences of L_{cr} and the folding and coiling frequencies on the liquid jet viscosity, its velocity and the nozzle diameter were established. Buckling was also observed in horizontal jets moving over the free surface of a denser liquid (such jets widen beginning from the nozzle, in distinction from gravity-driven jets, which initially become thinner and begin to widen only close to the wall onto which they impinge). All the observations confirmed the idea of Taylor [14] that buckling of liquid jets is determined by the presence of the longitudinal compressive force acting in the jet and in this sense is a direct analog of the elastic buckling of bars and columns studied by Euler [8]. A detailed theory of the onset of buckling instability (folding of highly viscous liquid jets and films-planar jets-impinging on a wall) was given by Yarin et al. in [1, 17, 18] based on the general quasi-one-dimensional equations of jet dynamics (2.2)–(2.19) (see also the later efforts directed on a nonlinear buckling theory in [19]).

Recently, jet buckling on laterally moving solid surfaces nearly perpendicular to the jet axis was reported [20–22], which is of interest, in particular, in relation to writing by short straight electrically driven jets. The stability analysis in that case was also based on the quasi-one-dimensional equations of the dynamics of liquid jets similar to (2.2)–(2.19). It revealed that the characteristic frequencies of buckling are practically unaffected by the lateral motion of the surface and stay the same as in the case of liquid jet impingement on a stationary hard flat surface [21, 22]. Moreover, the deposit morphology at the wall is practically unaffected by the method of jet initiation (gravity-driven jets [20] versus the electrically driven jets

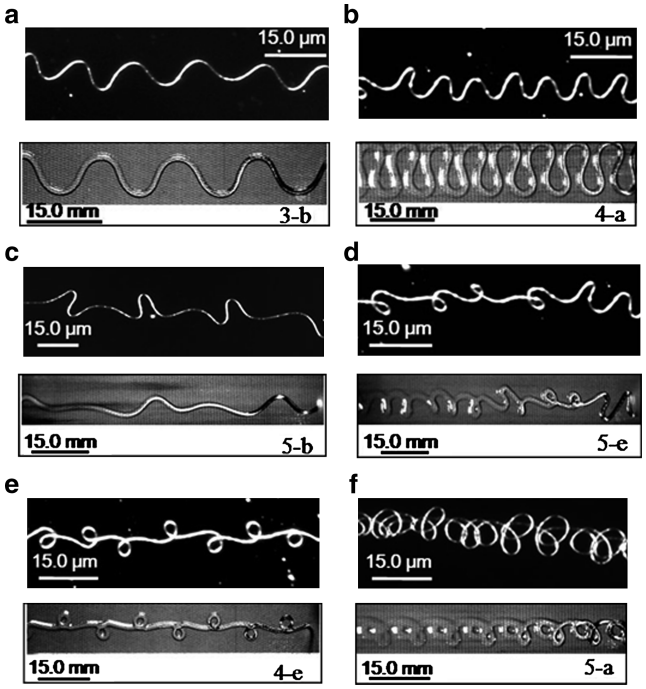

Fig. 2.6 (**a**–**f**) Comparison of the buckled patterns created by electrified jets of polyethylene oxide (*PEO*) in water, collected on glass slides in [22], to patterns produced by the buckling of the uncharged gravity-driven syrup jets [20]. Note that the gravity-driven syrup jets and their buckling patterns are about 1,000 times larger than those of the electrified jets of PEO in water. The upper panel in each pair depicts the results for the electrified PEO jets in [22]. The lower panels show the similar patterns produced by the syrup jets in [20]. The symbols in the lower right corner of each panel are the figure number found in [20] (Courtesy of Elsevier)

[22]) as Fig. 2.6 demonstrates. The buckling frequency ω predicted by the linear stability theory of Yarin et al. [1, 17]

$$\ln\left(\omega\frac{d_0}{V_0}\right) = -0.0194\ln\left(\frac{\mu Q}{\rho g d_0^4}\right) + 0.2582 \tag{2.28}$$

is in reasonable agreement with the experimental data for ω evaluated from the images similar to those in Fig. 2.6 (d_0 denotes the initial cross-sectional jet diameter, Q is the volumetric flow rate in the jet, and g is the gravity acceleration).

Bending Instability of Electrified Liquid Jets

The electrified jets of concentrated polymer solutions move in air with low speeds of the order of 1 m/s. However, they bend due to the Coulombic interactions discussed above in relation with the electric bending force (2.20). Such jets emerge

in electrospinning of polymer nanofibers, one of the nanotechnological processes [9–11, 23, 24]. Comparison of the expressions for the bending forces $\vec{q}$ in the aerodynamic and electric cases, (2.18) and (2.20), respectively, reveals that in the electrically driven bending instability the factor ${e_0}^2\ln(L/a_0)/\pi{a_0}^2$ plays the role of the factor $\rho_g U^2$ in the aerodynamic bending. Accounting for this analogy, it is easy to see that the electrospinning process is enabled by the fact that the viscoelastic stresses dominate the surface tension and prevent capillary breakup when the electric analog of (2.23)

$$\frac{\pi\mu^2}{\rho e_0^2 \ln(L/a_0)} \gg 1 \tag{2.29}$$

holds (e_0 denotes the initial electric charge per unit length of a straight jet). If polymer concentration is too low, capillary perturbations grow on the background of the bending perturbations, since the inequality does not hold, and nanofibers with beads are formed, which is also of interest in certain applications [11]. In the case of electrospinning, the stabilizing role of the viscoelastic stresses in the jet is the key element of the process, since it aims at production of intact nanofibers, in distinction from electrospraying, the process where liquid is fully atomized by the electric forces, which enhances capillary instability.

Several images of bending polymer jets in electrospinning are shown in Fig. 2.7.

The electrospinning jets typically have an almost straight section of the order of several cm followed by a number of bending loops shown in Fig. 2.7. The region near the vertex of the envelope cone about the bending loops in this figure was imaged at 2,000 frames per second. The stereographic images in Fig. 2.7 show the jet shape in three dimensions. The expanding spiral in this figure is a simple example of the kinds of paths that were observed in [9]. After a short sequence of unstable bending back and forth, with growing amplitude, the jet followed a bending, winding, spiraling, and looping path in three dimensions. The jet in each loop grew longer and thinner as the loop diameter and circumference increased. After some time, segments of a primary loop suddenly developed a new bending instability (secondary loops), similar to, but at a smaller scale than, the first

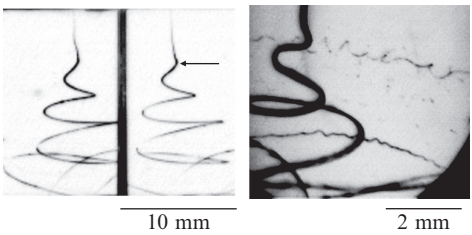

Fig. 2.7 *Left*: Stereographic images of an electrically driven bending instability. The exposure time was 0.25 ms. The *arrow* marks a maximum lateral excursion of a loop. *Right*: An enlarged image of the end of the straight segment of the jet. The exposure time was 0.25 ms (After [9]. Courtesy of AIP)

(cf. the smaller loops on the right-hand side image in Fig. 2.7, where the secondary loops superimposed on the primary ones are clearly seen). Each cycle of bending instability can be described in three steps. (1) A smooth segment that was straight or slightly curved suddenly developed primary bending loops. (2) The segment of the jet in each bend elongated and became a part of spiraling loops with growing diameters. (3) As the loop length increased, the cross-sectional diameter of the jet forming the loop grew smaller, the conditions for step (1) re-established on a smaller scale, and the next cycle of bending instability began resulting in the secondary loops. This cycle of instability was observed to repeat at an even smaller scale resulting in a fractal-like jet. The length of such a fractal jet increased enormously creating nanofibers. In a while, the polymer solution jet lost most of its solvent due to evaporation in flight, solidified as it dried, and electrospun nanofibers were collected at some distance below the envelope cone.

The instability mechanism that is relevant in the electrospinning context is illustrated by the Coulombic interaction of three point-like material elements, each with charge e, moving on a jet and originally in a straight line at A, B, and C as shown in Fig. 2.8. (It is emphasized that charge transport in such a jet is practically purely convective [11]). Two Coulomb forces having magnitudes $F = e^2/r^2$ (in the Gaussian units) push against charge B from opposite directions. If a bending perturbation causes the charged material element B to move off the line by a distance δ to B′, a net force $F_1 = 2F\cos\theta = (2e^2/r^3)\delta$ acts on charge B in the direction perpendicular to the line. This net force tends to cause B to move further in the direction of the bending perturbation away from the line between fixed charges, A and C. Then, the growth of the small bending perturbation that is characterized by δ is governed in the linear approximation by the second law of Newton according to the equation

$$m\frac{d^2\delta}{dt^2} = \frac{2e^2}{l_1^2}\delta \tag{2.30}$$

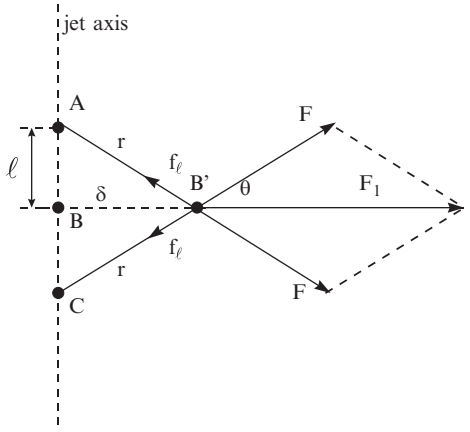

Fig. 2.8 Illustration of the instability, leading to bending of an electrified jet (After [9]. Courtesy of AIP)

where m is the mass, and ℓ is the initial separation between charges A and B in the straight jet.

The growing solution of this equation, $\delta = \delta_0 \exp[(2e^2/ml_1^3)^{1/2}t]$, shows that small perturbations increase exponentially. The increase is sustained because the electrostatic potential energy of the system shown in Fig. 2.8 decreases as e^2/r when the perturbations, characterized by δ and r, grow.

A detailed theory of the bending instability of the electrified polymer jets in electrospinning was given in [9, 10] (see also the reviews [11, 23, 24] and references therein). Recasting the inequality (2.22) for the onset of the aerodynamic bending reveals that the destabilizing electric force overcomes the stabilizing effect of the surface tension if

$$e_0^2 \ln\left(\frac{L}{a_0}\right) > \pi a_0 \sigma \tag{2.31}$$

The equation for the growth rate of small aerodynamic bending perturbations (2.21) is recast in the following equation for the electrically-driven bending [9, 10]

$$\gamma^2 + \frac{3}{4}\frac{\mu \bar{k}^4}{\rho a_0^2}\gamma + \left(\frac{\sigma}{\rho a_0^3} - \frac{e_0^2 \ln(L/a_0)}{\pi \rho a_0^4}\right)\bar{k}^2 = 0 \tag{2.32}$$

The corresponding wavenumber $\bar{k}_*$ and the growth rate γ_* of the fastest growing electrically-driven bending perturbation are given by

$$\bar{k}_* = \left\{\frac{8}{9}\frac{\rho a_0^2}{\mu^2}\left[\frac{e_0^2 \ln(L/a_0)}{\pi a_0^2} - \frac{\sigma}{a_0}\right]\right\}^{1/6} \tag{2.33}$$

$$\gamma_* = \frac{\left[e_0^2 \ln(L/a_0)/\pi a_0 - \sigma\right]^{2/3}}{\left(3\mu\rho a_0^4\right)^{1/3}} \tag{2.34}$$

with $\ln(L/a_0) = \ln(1/\bar{k}_*)$ [10].

The nonlinear stage of the electrically-driven bending instability in electrospinning was studied numerically in [9, 10] using the general quasi-one-dimensional equations of the dynamics of thin liquid jets described in Section "General Quasi-One-Dimensional Equations of Dynamics of Free Liquid Jets." In addition, in [10], the dynamic equations were supplemented by the equations describing solvent evaporation, jet solidification, and the effect of these processes on the rheological behavior of polymeric liquid. Figure 2.9 illustrates the predicted evolution of an electrospun jet.

The fact that strongly stretched polymeric jets are stable relative to bending perturbations demonstrated in [9] means that the electrospun jets possess an initial straight section. It also means that transversal waves can propagate over a stretched jet as over a string [25, 26] (Fig. 2.10). The widening of a lateral displacement pulse

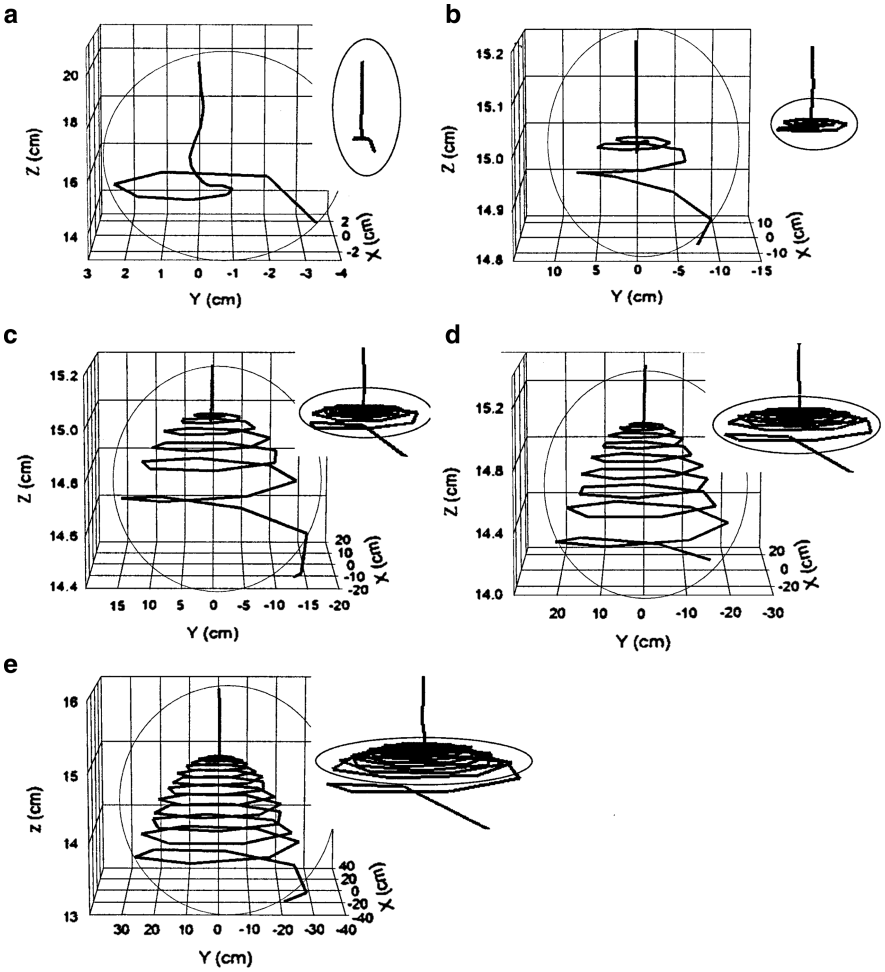

Fig. 2.9 Bending instability of a single jet. Only the jet axis is shown at the dimensionless time moments: (**a**) 0.19, (**b**) 0.39, (**c**) 0.59, (**d**) 0.79, and (**e**) 0.99 (After [9]. Courtesy of AIP)

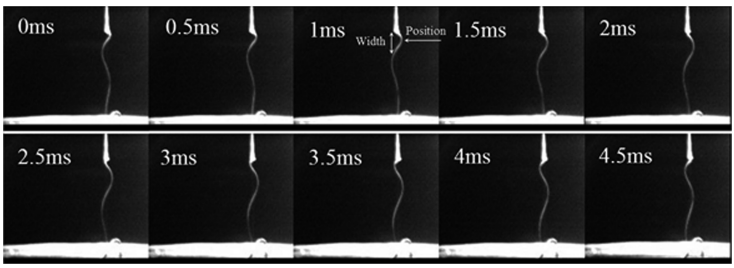

Fig. 2.10 Propagation and widening of a single lateral displacement pulse on an electrically-driven jet of a concentrated polymer solution [26]. The interelectrode distance $L = 5.5$ cm, potential difference of $U = 3$ kV, and the electric current $I = 100$ nA. The jet was straight before the lateral displacement pulse was applied by a plastic impactor (Courtesy of Elsevier)

W between $t = 0$ and $t = \Delta t$ can be measured from such images. Then, the longitudinal stress in the polymeric jet is recovered as

$$\sigma_{xx} = \rho\left(\frac{W}{2\Delta t}\right)^2 \tag{2.35}$$

An elongational rheometer developed in [26] based on this principle revealed that the initial longitudinal stress created by the electric stretching of a polymeric jet as it transforms from the modified Taylor cone to a thin jet, is of the order of 10–100 kPa. These values are one or two orders of magnitude larger than those measured for the uncharged viscoelastic jets. The rheometer also allows evaluation of the modulus of elasticity and relaxation time of concentrated polymer solutions and melts.

References

1. Yarin, A. L. *Free Liquid Jets and Films: Hydrodynamics and Rheology*. Longman, Wiley & Sons; Harlow/New York: Longman/Wiley (1993).
2. Weber, C. On the breakdown of a fluid jet, Zum Zerfall eines Flussigkeitsstrahles, *Z. Angrew. Math und Mech*., 11, 136–154 (1931).
3. Debye, P. & Daen, J. Stability considerations of nonviscous jets exhibiting surface or body tension. *Phys. Fluids* 2, 416–421 (1959).
4. Grant, E. M. & Middleman, S. Newtonian jet stability. *AIChE J*. 12, 669–678 (1966).
5. Entov, V. M. & Yarin, A. L.: Dynamical equations for a liquid jet. *Fluid Dyn*. 15, 644–649 (1980).
6. Entov, V. M. & Yarin, A. L. The dynamics of thin liquid jets in air. *J. Fluid Mech*. 140, 91–111 (1984).
7. Yarin, A. L. On the dynamical equations for liquid jets. *Fluid Dyn*. 18, 134–136 (1983).
8. Landau, L. D. & Lifshitz, E. M. *Theory of Elasticity* Pergamon, New York (1975).
9. Reneker, D. H. Yarin, A. L. Fong, H. & Koombhongse, S. Bending instability of electrically charged liquid jets of polymer solutions in electospinning. *J. Appl. Phys*. 87, 4531–4547 (2000).
10. Yarin, A. L. Koombhongse, S. & Reneker, D. H. Bending instability in electrospinning of nanofibers. *J. Appl. Phys*. 89, 3018–3026 (2001).
11. Reneker, D. H. Yarin, A. L. Zussman, E. & Xu, H. Electrospinning of nanofibers from polymer solutions and melts. *Adv. Appl. Mech*. 41, 43–195 (2007).
12. Bresee R. R. & Ko, W. C. Fiber formation during melt blowing. *Int. Nonwovens J*., 21–28, Summer (2003).
13. Taylor, G. I. Instability of jets, threads and sheets of viscous fluid. In: Proceedings of the 12th International Congress Appl. Mech., Stanford, 1968. Stanford, pp. 382–388 (1969).
14. Taylor, G. I. Electrically driven jets. *Proc. R. Soc. Lond*. A313, 453–475 (1969).
15. Cruickshank J. O. & Munson, B.R. Viscous fluid buckling of plane and axisymmetric jets. *J. Fluid Mech*. 113, 221–239 (1981).
16. Munson, B. R. Viscous buckling of slender horizontal jets. *Phys. Fluids* 24, 1780–1783 (1981).
17. Tchavdarov, B. Yarin, A. L. & Radev, S. Buckling of thin liquid jets. *J. Fluid Mech*. 253, 593–615 (1993).
18. Yarin A. L. & Tchavdarov, B. Onset of folding in plane liquid films. *J. Fluid Mech*. 307, 85–99 (1996).

19. Skorobogatiy M. & Mahadevan, L. Folding of viscous sheets and filaments. *Europhys. Lett*. 52, 532–538 (2000).
20. Chiu-Webster S. & Lister, J. R. The fall of a viscous thread onto a moving surface: a 'fluid-mechanical sewing machine'. *J. Fluid Mech*. 569, 89–111 (2006).
21. Ribe, N. M. Lister, J. R. & Chiu-Webster, S. Stability of a dragged viscous thread: onset of 'stitching' in a fluid-mechanical 'sewing machine'. *Phys. Fluids* 18, 124105 (2006).
22. Han, T. Reneker, D. H. & Yarin, A. L. Buckling of jets in electrospinning. *Polymer* 48, 6064–6076 (2007).
23. Yarin, A. L. Zussman, E. Wendorff, J. H. & Greiner, A. Material encapsulation in core-shell micro/nanofibers, polymer and carbon nanotubes and micro/nanochannels. *J. Mater. Chem*. 17, 2585–2599 (2007).
24. Reneker D. H. & Yarin, A. L. Electrospinning jets and polymer nanofibers. *Polymer* 49, 2387–2425 (2008).
25. Goren S. & Gavis, J. Transverse wave motion on a thin capillary jet of a viscoelastic liquid. *Phys. Fluids* 4, 575–579 (1961).
26. Han, T. Yarin, A. L. & Reneker, D. H. Viscoelastic electrospun jets: initial stresses and elongational rheometry. *Polymer* 49, 1651–1658 (2008).

http://www.springer.com/978-1-4419-7263-7

Handbook of Atomization and Sprays
Theory and Applications
Ashgriz, N. (Ed.)
2011, XVI, 936 p., Hardcover
ISBN: 978-1-4419-7263-7